JGR Solid Earth

RESEARCH ARTICLE
10.1029/2019JB017436

# The Influence of Water on the Strength of Olivine Dislocation Slip Systems

**Jacob Tielke[1,2,3], Julian Mecklenburgh[4], Elisabetta Mariani[1], and John Wheeler[1]**

[1]Department of Earth, Ocean and Ecological Sciences, University of Liverpool, Liverpool, UK, [2]Lunar and Planetary Institute, Houston, TX, USA, [3]Astromaterials Research and Exploration Science, NASA Johnson Space Center, Houston, TX, USA, [4]School of Earth and Environmental Sciences, The University of Manchester, Manchester, UK

**Key Points:**
- All investigated olivine dislocation slip systems exhibit hydrolytic weakening
- The strength of the (001)[100] slip system is most sensitive to water fugacity
- The different sensitivities of slip systems to water fugacity may explain the different LPO types observed in mantle rocks

**Correspondence to:**
J. Tielke,
jacob.a.tielke@nasa.gov

**Citation:**
Tielke, J., Mecklenburgh, J., Mariani, E., & Wheeler, J. (2019). The influence of water on the strength of olivine dislocation slip systems. *Journal of Geophysical Research: Solid Earth*, *124*, 6542–6559. https://doi.org/10.1029/2019JB017436

Received 25 JAN 2019
Accepted 8 JUL 2019
Accepted article online 11 JUL 2019
Published online 26 JUL 2019

**Abstract** The nature of lattice-preferred orientation (LPO) in olivine-rich rocks strongly influences many important physical properties of Earth's upper mantle. Different LPO types have been observed to develop in deformation experiments on olivine-rich rocks carried out at different water fugacity conditions. The development of the different LPO types has been attributed to dislocation slip systems in olivine having different sensitivities to water fugacity, but this hypothesis has not been directly tested. To measure the influence of water fugacity on the relative strengths of olivine dislocation slip systems, we carried out a series of deformation experiments on olivine single crystals under either anhydrous or hydrous conditions. The crystals were oriented to activate either the (010)[100], (001)[100], or (100)[001] dislocation slip systems using a direct shear geometry, which allows for isolation of single slip systems, in contrast to the multiple systems activated in experiments carried out in compression. Post-deformation electron backscatter diffraction analyses reveal orientation gradients consistent with deformation occurring via the motion of dislocations on the activated slip systems. Crystals in all of the investigated orientations exhibit hydrolytic weakening, but crystals oriented to activate the (001)[100] slip system exhibit the largest degree of weakening. These results are consistent with a water-induced change in LPO in olivine-rich rocks deforming by dislocation creep. The rheological data obtained from the experiments can be used to improve models of LPO evolution in Earth's mantle, which is critical for imaging the structure of Earth's interior and predicting the movement of Earth's tectonic plates.

## 1. Introduction

The nature of lattice-preferred orientation (LPO) of olivine in peridotites strongly influences the physical properties of Earth's mantle. The velocity of seismic waves in mantle rocks are strongly dependent on the orientation of their constituent grains (e.g., Hess, 1964; Ismail & Mainprice, 1998; Nicolas & Christensen, 1987; Raitt, 1969). Deformation experiments and numerical simulations on olivine-rich rocks illustrate the importance of LPO in controlling viscous anisotropy in Earth's mantle (e.g., Boneh et al., 2015; Hansen et al., 2016). Electrical conductivity in mantle rocks is influenced by water not just by its direct effect in altering lattice defect concentrations (Poe et al., 2010) but also by its effect on slip systems, which influence LPO development; LPO in turn influences conductivity (Pommier et al., 2018). These examples highlight the need for robust models of the influence of water on LPO development in mantle rocks.

A variety of different LPO types have been observed in naturally and experimentally deformed olivine-rich rocks and aggregates as presented in Figure 1. These different LPO types describe the distribution of the principal crystallographic axes of individual grains with respect to an imposed deformation geometry. The dependence of LPO type and strength on intracrystalline water content of olivine aggregates is well established (e.g., Jung & Karato, 2001; Jung et al., 2006; Katayama & Karato, 2008). These different LPO types have also been observed in exposures of mantle rocks (e.g., Jung et al., 2013; Michibayashi & Oohara, 2013; Tasaka et al., 2008) and xenoliths (Park & Jung, 2015) and have been used to interpret water concentrations in regions of the mantle based on observations of seismic anisotropy (Karato et al., 2008; Kneller et al., 2005, 2007). However, the microphysical mechanisms that give rise to the development of the different LPO types is not well understood. One hypothesis that has yet to be fully tested is that the dislocation slip systems in olivine weaken by different amounts in response to changes in water concentration (e.g., Mackwell et al., 1985; Skemer et al., 2013; Wallis et al., 2019; Wang et al., 2019).

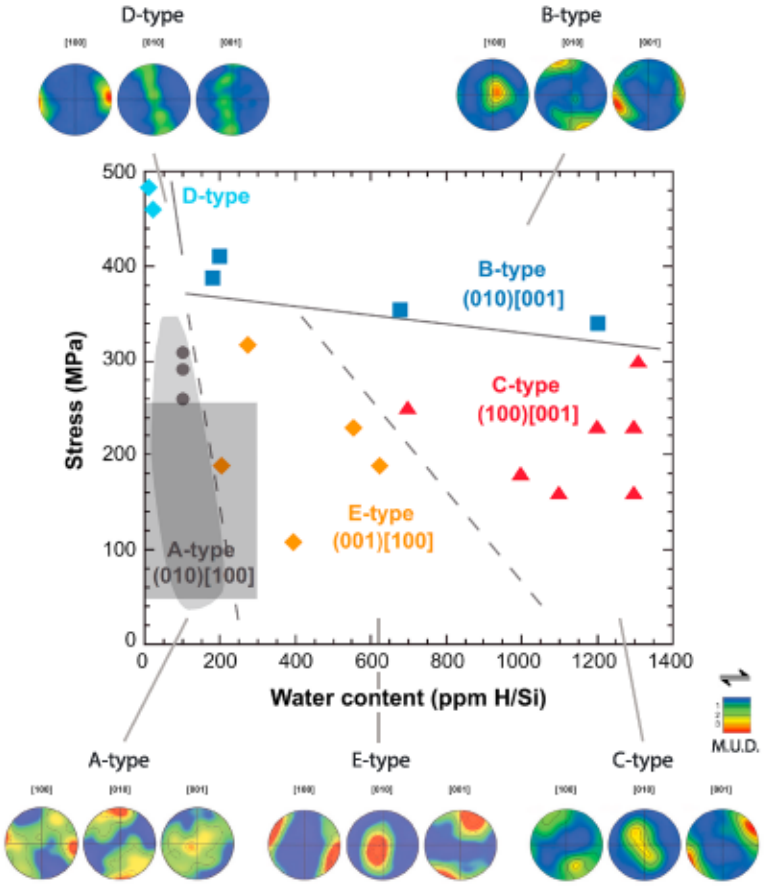


**Figure 1.** Lattice-preferred orientation (LPO) diagram modified from Karato et al. (2008), illustrating the different LPO types observed to occur during experimental deformation of olivine aggregates under different conditions of stress and water content. The conditions of the current study are represented by the gray box that occupies part of the A-type and E-type LPO domains. The scale for the contouring of the pole figures in multiples of uniform distribution (M.U.D.) and sense of shear are in the bottom right of the diagram.

The current lack of knowledge about the mechanisms leading to the development of different LPOs in olivine at different water contents highlights the need for systematic measurements of the relative strength of the different olivine dislocation slip systems at different water concentrations. The most direct means of measuring the strength of dislocation slip systems is through analysis of single-crystal deformation experiments (e.g., Bai et al., 1991; Durham & Goetze, 1977; Girard et al., 2013; Kohlstedt & Goetze, 1974; Mackwell et al., 1985; Raterron et al., 2007, 2009; Tielke, Zimmerman, et al., 2016, 2017). Single-crystal experiments allow for direct measurements of the viscous response of dislocation slip systems while avoiding the complexity of grain boundaries and crystallographic texture development in polycrystalline materials.

In this study we carried out experiments under both anhydrous and hydrous conditions to measure the deformation rates of olivine single crystals deforming by the motion of dislocations on different slip systems. We used a direct shear geometry (e.g., Holtzman et al., 2003; Tielke, Zimmerman, et al., 2016; Zhang & Karato, 1995), as exemplified in Figure 2. The direct shear geometry allows for isolation of the (001)[100] and (100)[001] dislocation slip systems, which cannot be measured individually using traditional compression experiments (e.g., Bai et al., 1991; Mackwell et al., 1985) but are proposed to have different water sensitivities (Jung et al., 2006). The mechanical and microstructural data from this study can be compared to physical models of dislocation motion, to elucidate the underlying processes controlling dislocation motion and hydrolytic weakening on olivine slip systems.

The climb-controlled model of dislocation creep describes a material deforming by the motion of dislocations where most of the strain is achieved by the glide of dislocations, but the strain rate is limited by the rate at which dislocations climb to overcome obstacles such as other dislocations (e.g., Weertman, 1955). Climb

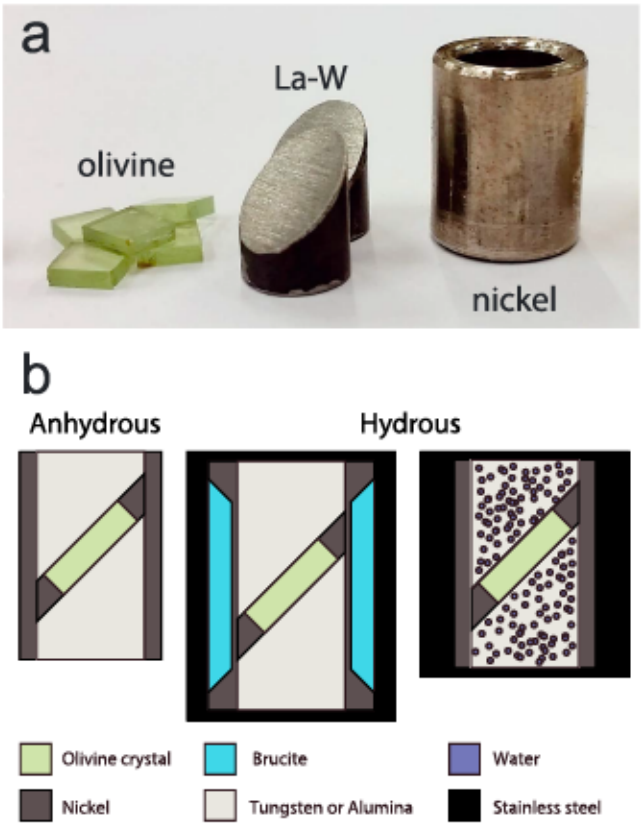


**Figure 2.** (a) Example of oriented sections of olivine crystals, lanthanated tungsten pistons (La-W), and nickel sleeve used for shear experiments. The La-W pistons are 6.5 mm in diameter. (b) Illustrations of deformation geometries used in the study. Left: assembly used for anhydrous experiments. Center and right: assemblies used in hydrous experiments.

is controlled by the rate of diffusion of the slowest moving species by the fastest diffusion mechanism. Silicon is the slowest diffusing species in olivine and is influenced by the concentrations of vacancies and other types of point defects, which in turn are controlled by the amounts of impurities such as structurally incorporated hydrogen (e.g., Dohmen et al., 2002; Kohlstedt, 2006). Materials deforming by climb-controlled creep exhibit a power law dependence of strain rate, $\dot{\gamma}$, on stress, $\tau$, and an Arrhenius dependence on temperature, such that

$$\dot{\gamma} = A\tau^n \exp\left(\frac{-Q}{RT}\right), \tag{1}$$

where $A$ is a material specific constant, $n$ is the stress exponent, $Q$ is the activation energy, R is the gas constant, and $T$ is the temperature in kelvin. For olivine deforming under hydrous conditions, values of $n$ generally vary between 2 and 3 (Chopra & Paterson, 1984; Karato et al., 1986; Mackwell et al., 1985; Tielke et al., 2017), consistent with deformation that is controlled by the rate of climb that is rate limited by lattice diffusion of silicon (Hirth & Kohlstedt, 2015). Values of $n$ range from ~3 to ~5 for olivine deforming under anhydrous conditions, which is more consistent with climb that is rate limited by diffusion of silicon along the cores of dislocations (Hirth & Kohlstedt, 2015). Hydrolytic weakening in the climb-controlled regime likely occurs by an increase in silicon diffusion rates that results from the increase in silicon vacancies that form in response to hydrogen entering the olivine lattice as a charged defect (Mei & Kohlstedt, 2000).

The glide-controlled model of dislocation creep describes a material deforming by the motion of dislocations that are rate limited by impediments to glide such as lattice resistance (e.g., Frost & Ashby, 1982; Poirier, 1985). Materials deforming by glide-controlled creep obey an exponential dependence of strain rate on stress and follow a modified Arrhenius relationship:

$$\dot{\gamma} = A\tau^n \exp\left[\left(\frac{-Q}{RT}\right)\left(1-\left(\frac{\tau}{\tau_p}\right)^p\right)^q\right], \tag{2}$$

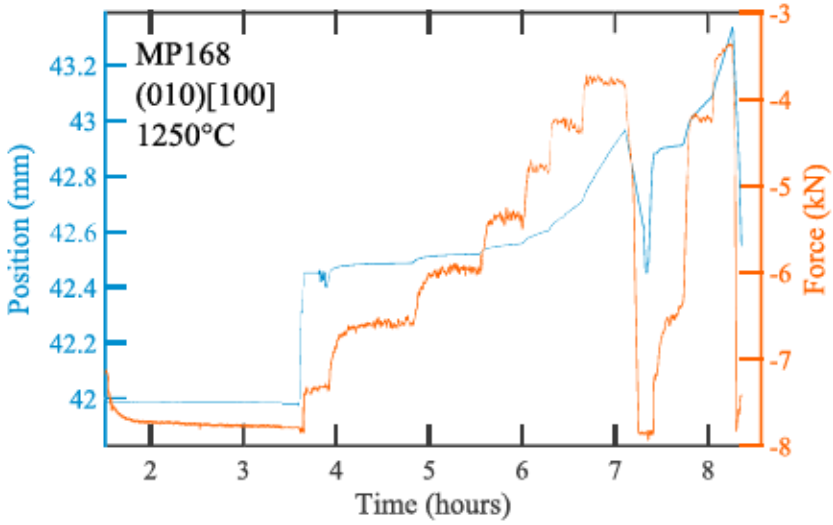


**Figure 3.** Mechanical data from Experiment MP168. The red line corresponds to the value of force in kilonewtons measured with the internal force gauge. The blue lines are the value of position, which changes in response to the applied force and is measured using an external linear voltage displacement transducer.

where $\tau_p$ is the stress needed to overcome obstacles and $p$ and $q$ describe the shape of the obstacles. Values of $n$, $\tau_p$, $p$, and $q$ in the glide-controlled regime vary significantly between studies (e.g., Demouchy et al., 2013; Evans & Goetze, 1979; Idrissi et al., 2016; Katayama & Karato, 2008; Kumamoto et al., 2017). Hydrolytic weakening in a glide-controlled regime may occur as a result of the interaction of hydrogen ions with adjacent bonds in the crystal lattice, which makes them easier to break and results in lower values of $\tau_p$ (Griggs, 1967; Skelton & Walker, 2018; Wang et al., 2019). In olivine, it is generally agreed that glide-controlled creep is more important at low-temperature and/or high-stress conditions (e.g., Evans & Goetze, 1979; Katayama & Karato, 2008; Kumamoto et al., 2017; Tielke et al., 2017). However, recent experimental evidence suggests that it may also operate at high-temperature and low-stress conditions (Cooper et al., 2016).

By comparing the strength of the different slip systems under different conditions, we can compare the amount of weakening on each slip system introduced by adding hydrogen to the olivine lattice. Lastly, by comparing mechanical data and microstructure of the deformed material, we can evaluate the models of hydrolytic weakening for olivine deforming by dislocation creep. Ultimately, these data can be used to improve models of LPO evolution in Earth's mantle, which is critical for understanding both the structure of Earth's interior and the movement of Earth's tectonic plates.

## 2. Methods

### 2.1. Experimental Design

The starting material in this study consisted of single crystals of olivine from Pakistan that were nearly free of optically observable inclusions. Two large crystals were oriented using electron backscatter diffraction (EBSD) and sliced into sections 1 mm thick with orientations to activate the (010)[100], (001)[100], or (100)[001] slip systems using a direct shear geometry. The direct shear geometry restricts the motion of the slip system with a Burgers vector that is normal to the shear plane. Experiments were also attempted on crystals oriented for the (010)[001] slip system but required high shear stress and resulted in slipping between the crystals and the shear pistons. The slices were cleaned using acetone in an ultrasonic bath, positioned between pistons of either lanthanated tungsten or alumina, and placed in a nickel sleeve as presented in Figure 2. Both the crystals and the shear pistons were abraded to create shallow scratches perpendicular to the directions of shear to increase the frictional properties of the interface between the crystal and the shear pistons. For experiments carried out under hydrous conditions, water (which dissociates at our experimental conditions) was supplied to the crystals by placing mixtures of brucite and talc on the outside of a thin-walled nickel sleeve inside of the capsule. This material forms a very weak material with high-porosity upon dehydration and has a negligible effect on the mechanical properties of the assembly. An alternative design was used for Experiment MP178, where water was supplied by placing deionized water in the pore spaces of the porous alumina pistons that were separated from the crystal by a thin tungsten foil. In the first

case, hydrogen, dissociated from water, diffuses through the thin nickel sleeve and enters the olivine crystal. In the second case, dissociation occurs within the pore spaces of the alumina pistons and enters the lattice of the olivine crystal. In all cases, olivine is in contact with nickel and tungsten and is therefore exposed to the same chemical environment. Stainless steel capsules used in hydrous experiments were sealed using a Lampert PUK 3 tungsten inert gas welder.

### 2.2. Deformation Experiments

Deformation experiments were carried out using the Paterson gas-medium apparatus (Paterson, 1990) at the University of Manchester. Argon gas was used as a confining medium, and temperature was controlled via a R-type thermocouple placed next to the sample and inside of a precalibrated resistive heating furnace. At the beginning of each experiment, temperature and pressure were held constant for 2 hr before deformation was carried out using a series of constant force steps. Shear stresses were calculated using $\tau = \frac{1}{\sqrt{2}}\frac{F}{A}$, where $F$ is the measured axial force and $A$ is the area of the crystal in contact with one of the shear pistons. Shear strain rates were calculated by $\dot{\gamma} = \sqrt{2}\frac{\dot{d}}{t}$, where $\dot{d}$ is the measured axial displacement rate and $t$ is the thickness of the crystal.

During each force step, the force was held constant until the change in displacement rate as a function of time became negligible. Multiple load steps were applied during each experiment and earlier load steps were repeated at the end of the experiments to assess the possible influence of evolving microstructure and changes in hydrogen content on the mechanical behavior, as presented in Figure 3. Some lower force steps did not achieve quasi steady-state behavior and were omitted from analyses. Mechanical data were corrected for the stress supported by the metal jackets using published flow laws for nickel and gamma-iron from Frost and Ashby (1982) and for stainless steel using measurements described in Appendix A.

### 2.3. EBSD Analyses

Postdeformation EBSD analyses were carried out using a X500 CrystalProbe CamScan field emission gun scanning electron microscope at the University of Liverpool with 20-kV accelerating voltage, 30-nA beam current, and a spot size of 5.3 nm. The capsule containing the crystal and shear pistons was cut in the plane containing the shear direction and the direction of applied force. The samples were then polished using diamond lapping film with sequentially smaller grain diameters ranging from 30 to 1 μm before polishing in a solution containing colloidal silica for 30 min. The samples were dried on a hot plate before applying a thin coat of carbon to avoid charging during scanning electron microscope analyses. AZtec software was used for EBSD acquisition and processing was carried out using MTEX (Bachmann et al., 2010) and Crystalscape software (Wheeler et al., 2009).

### 2.4. FTIR Analyses

Fourier-Transform Infrared Spectroscopy (FTIR) analyses were carried out using a PerkinElmer Spotlight 400 in transmitted light mode at the University of Manchester. The analyses were performed on samples hydrated using the assembly in Figure 2, but with polycrystalline olivine pistons. This assembly avoided excess fracturing during quenching. Fracturing was a result of differences in thermal expansion between olivine and lanthanated tungsten that presented challenges when preparing doubly polished samples, thus hampering quantitative FTIR measurements on sheared crystals. Samples were prepared for FTIR by creating sections parallel to the (010) crystallographic plane. The sides of the samples were polished as per preparing EBSD analyses but without the use of a colloidal silica solution, to a thickness of 0.5 mm. The samples were dried overnight in a vacuum oven prior to analysis. Values of absorbance of unpolarized infrared beam were acquired for wavenumbers of 400 to 4,000 $cm^{-1}$ by averaging over 128 scans collected at a resolution of 2 $cm^{-1}$ and using a 100 × 100-μm window. Hydrogen concentration was calculated by integrating the region beneath baseline-corrected FTIR spectra using the method of Paterson (1982) multiplied by a factor of 3.5 as suggested by Bell et al. (2003).

### 2.5. EPMA Analyses

Electron probe microanalyses (EPMA) were carried out to quantify the composition of the starting materials using a Cameca SX 100 electron microprobe at the University of Manchester. Wavelength dispersive spectroscopy data for Mg, Fe, and Si were collected using an accelerating voltage of 15 keV and a current of 7 nA and were calculated by comparing the k-alpha peaks on thallium acid pthalate and lithium fluoride (LIF) spectrometer signals to those of periclase (for Mg) and fayalite (for Fe and Si) standards with known compositions. Similarly, wavelength dispersive spectroscopy data for Al, Ca, Ti, Ni, Mn, and Al were collected using

**Table 1**
*Mechanical Data for Olivine Single Crystals*

| Exp.#, orientation | $\tau$ (MPa) | $\dot{\gamma}$ ($s^{-1}$) | Temperature (°C) | $\gamma^a$ | Wet/dry |
|---|---|---|---|---|---|
| MP167, (010)[100] | 99.43 | 2.88E−5 | 1250 | 0.02 | Dry |
| MP168, (010)[100] | 62.75 | 4.33E−6 | 1250 | 0.01 | Dry |
| | 84.62 | 1.26E−5 | 1250 | 0.01 | Dry |
| | 103.04 | 4.49E−5 | 1250 | 0.02 | Dry |
| | 119.18 | 9.14E−5 | 1250 | 0.06 | Dry |
| | 136.76 | 1.87E−4 | 1250 | 0.27 | Dry |
| | 121.51[b] | 1.26E−4 | 1250 | 0.07 | Dry |
| | 149.16 | 4.45E−4 | 1250 | 0.04 | Dry |
| MP178, (010)[100] | 62.80 | 4.12E−5 | 1250 | 0.02 | Wet |
| | 70.57 | 5.17E−5 | 1250 | 0.05 | Wet |
| | 77.51 | 6.55E−5 | 1250 | 0.06 | Wet |
| | 79.44 | 9.62E−5 | 1250 | 0.11 | Wet |
| | 75.29[b] | 8.60E−5 | 1250 | 0.04 | Wet |
| | 79.26 | 1.17E−4 | 1250 | 0.05 | Wet |
| | 81.94 | 1.64E−4 | 1250 | 0.17 | Wet |
| MP183, (100)[001] | 46.65 | 4.87E−5 | 1300 | 0.01 | Wet |
| | 53.15 | 5.68E−5 | 1300 | 0.02 | Wet |
| | 62.50 | 1.02E−4 | 1300 | 0.03 | Wet |
| | 70.43 | 1.35E−4 | 1300 | 0.09 | Wet |
| | 72.71 | 1.69E−4 | 1300 | 0.08 | Wet |
| | 75.77 | 2.08E−4 | 1300 | 0.06 | Wet |
| | 82.75 | 3.28E−4 | 1300 | 0.17 | Wet |
| | 87.19 | 3.75E−4 | 1300 | 0.16 | Wet |
| | 73.64[b] | 1.62E−4 | 1300 | 0.07 | Wet |
| MP186, (001)[100] | 21.91 | 4.77E−5 | 1300 | 0.01 | Wet |
| | 29.55 | 8.70E−5 | 1300 | 0.01 | Wet |
| | 22.28[b] | 3.43E−5 | 1300 | 0.01 | Wet |
| | 32.38 | 1.28E−4 | 1300 | 0.04 | Wet |
| | 35.64 | 2.07E−4 | 1300 | 0.02 | Wet |
| | 35.50 | 2.77E−4 | 1300 | 0.02 | Wet |
| | 37.62 | 4.25E−4 | 1300 | 0.03 | Wet |
| MP223, (001)[100] | 44.57 | 7.60E−6 | 1300 | 0.01 | Dry |
| | 54.17 | 1.06E−5 | 1300 | 0.01 | Dry |
| | 65.06 | 3.68E−5 | 1300 | 0.05 | Dry |
| | 72.58 | 6.12E−5 | 1300 | 0.02 | Dry |
| | 79.31 | 1.06E−4 | 1300 | 0.04 | Dry |
| | 60.16[b] | 4.06E−5 | 1300 | 0.01 | Dry |
| | 68.17[b] | 6.88E−5 | 1300 | 0.02 | Dry |
| | 75.00[b] | 1.13E−4 | 1300 | 0.01 | Dry |
| | 83.68 | 1.38E−4 | 1300 | 0.02 | Dry |

[a]Strains indicate steady-state shear strain achieved for each force step. [b]Lower force steps performed to check for strain hardening.

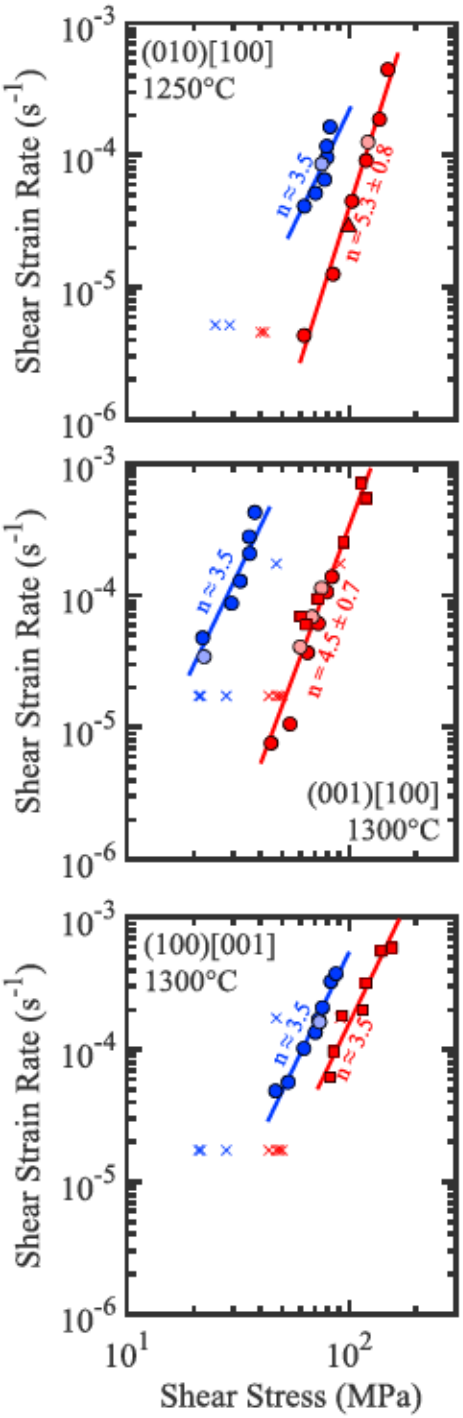


**Figure 4.** Mechanical data for crystals oriented to deform on the (010)[100] slip system (top), the (001)[100] slip system (center), and the (100)[001] slip system (bottom). All data points and results of least square fitting to data are corrected for the stress supported by the metal jackets. Data from anhydrous experiments are represented in red, data from hydrous experiments in blue, and lighter colored symbols indicate repeated loads to check for strain hardening. Circles and triangles are the data from Table 1, and squares are from Tielke, Zimmerman, et al. (2016). Crosses are from Mackwell et al. (1985) with crystals deformed in the $[110]_c$ orientation plotted on the top plot and those deformed in the $[101]_c$ orientation plotted on both the center and bottom plots. The data from Mackwell et al. (1985) are plotted as shear values, converted using the relationship in Appendix A, and data from $[110]_c$ experiments were approximated to 1250 °C using the activation energies for wet and dry olivine deforming by dislocation creep from Hirth and Kohlstedt (2003).

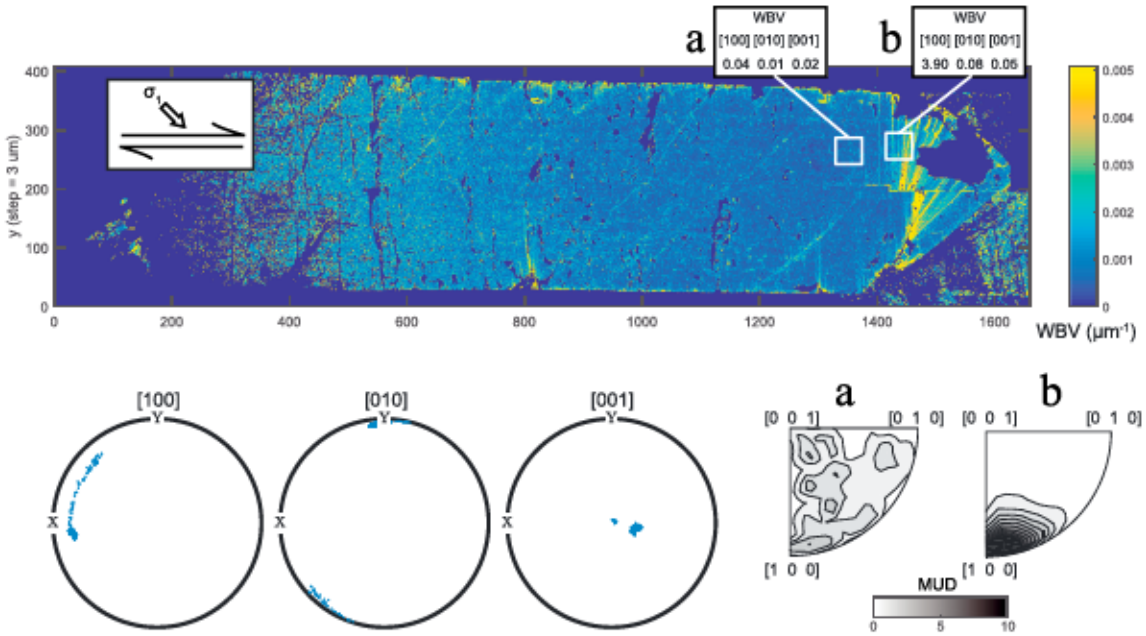


**Figure 5.** Map (top) and associated pole figures (bottom) of the Weighted Burgers Vector (WBV; Wheeler et al., 2009) from MP168, which was deformed under anhydrous conditions to activate the (010)[100] slip system. Yellow regions represent higher values of the WBV, indicating a higher density of geometrically necessary dislocations. The principal crystallographic axes are presented in the pole figures on the bottom left and inverse pole figures with the orientation of the WBV for the two regions (a and b) in the map are displayed in the bottom right. A weak preference for dislocations with $b = [100]$ is present in most of the crystal, whereas a strong concentration of dislocations with $b = [100]$ occurs in the low-angle boundaries that form on the edge of the crystal.

an accelerating voltage of 15 keV and a current of 50 nA and were calculated by comparing the k-alpha peaks on thallium acid pthalate, LIF, large LIF, and large pentaerythritol spectrometer signals to those of potassium feldspar (for Al), wollastonite (for Ca), rutile (for Ti), nickel oxide (for Ni), and tephronite (for Mn) standards. At least 25-point analyses carried out over a regularly spaced grid were collected. Point analyses that resulted in oxide wt% totals with greater than 1% deviation from 100% were omitted from consideration.

## 3. Results

### 3.1. Mechanical Data

Mechanical data from deformation experiments carried out under either anhydrous or hydrous conditions are presented in Table 1. The experiments were carried out at temperatures of 1250 to 1300 °C, a confining pressure of 300 MPa, shear stresses of 22 to 149 MPa, and resultant shear strain rates of $4.3 \times 10^{-6}$ to $4.4 \times 10^{-4}$ $s^{-1}$. For all orientations and for a given shear stress, crystals deformed under hydrous conditions deform at faster shear strain rates than those deformed under anhydrous conditions.

The repeated force steps in Table 1 reveal no evidence of strain hardening and therefore that there is no measurable water loss during our experiments. The lack of strain hardening also confirms that the intended slip system was activated, as activation of secondary slip systems would result in a decrease in Schmid factor with increasing strain. The crystals also retained their thickness after deformation, further confirming that only the intended slip system was activated during each experiment.

The mechanical behavior of crystals deformed under either anhydrous or hydrous conditions is consistent with the operation of a power law dependence of strain rate upon stress, as presented in Figure 4. Results of a least squares fit of the data for crystals deformed under anhydrous conditions reveals values of $n$ ranging from ~3.5 to 5.3. In contrast, fits of the data for crystals deformed under hydrous conditions are consistent with lower values of $n$. However, the small range of shear stresses and shear strain rates in this study results in considerable uncertainties in $n$. Therefore, a constant value of 3.5 was used for comparing the strain rate under either anhydrous or hydrous conditions for some of the results presented in Figure 4.

### 3.2. EBSD Analyses

EBSD analyses reveal the development of orientation gradients in deformed samples. Crystals deformed under anhydrous conditions and oriented for slip on the (010)[100] slip system exhibit low degrees of

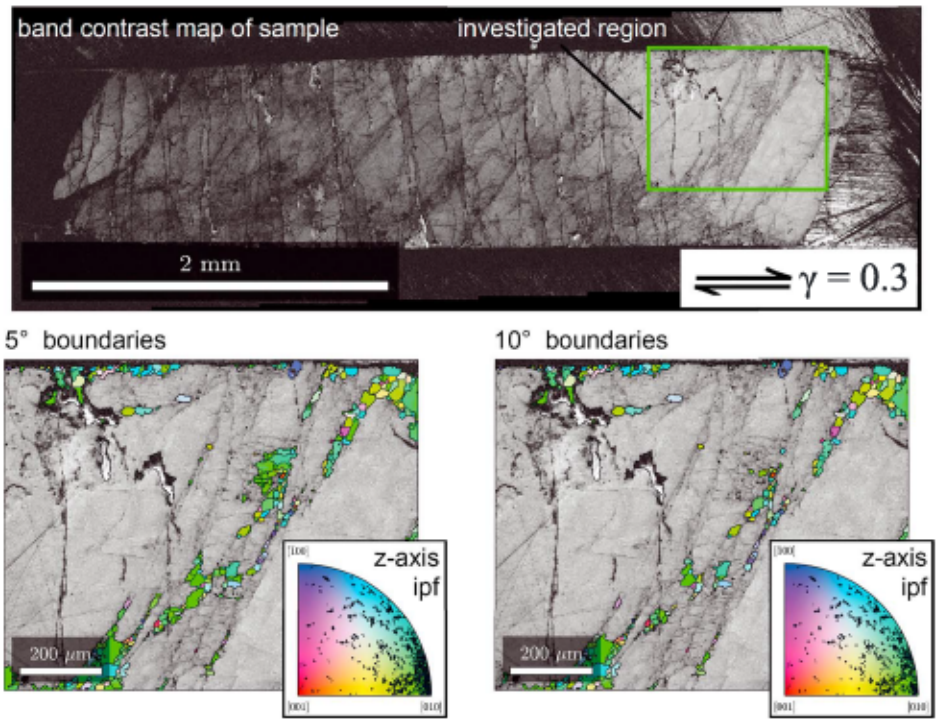


**Figure 6.** EBSD maps and inverse pole figures from MP183, which was oriented for deformation on the (100)[001] dislocation slip system. Localized dark regions in the band contrast map (top) are revealed to be small grains in higher magnification maps and segmenting EBSD data by 5° (bottom left) and 10° (bottom right). The orientation of the grains in the bottom two images are plotted on the *z* axis inverse pole figures. The small grains have a large range of orientations, with a weak preference that is similar to the original crystal (i.e., parallel to the [010] axis in the *z* axis inverse pole figure). EBSD = electron backscatter diffraction.

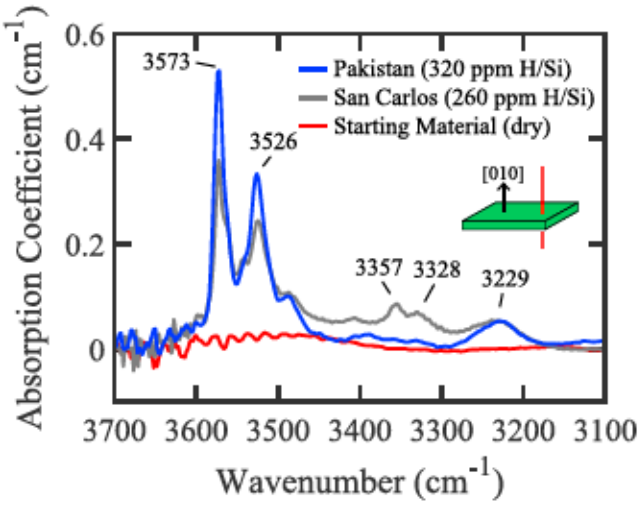


**Figure 7.** Results of FTIR analyses using an unpolarized infrared beam parallel to the [010] axis. The Olivine from Pakistan used in this study (blue) displays similar peak positions and heights to that of San Carlos olivine (gray) that was exposed to similar experimental conditions in Tielke et al. (2017). The starting material of natural olivine from Pakistan (red) is essentially anhydrous as is most olivine from San Carlos Arizona. The similarities in FTIR spectra for olivine annealed under hydrous conditions from the two different locations suggest that water is incorporated via similar mechanisms for olivine from San Carlos, Arizona, and Pakistan. FTIR = Fourier-Transform Infrared Spectroscopy.

misorientation throughout the volume of the crystal and the development of low-angle boundaries forming radiating structures at the edge of crystals, as exemplified in Figure 5. Examination of orientation gradients in the interior of these crystals using the Weighted Burgers Vector (WBV) method of Wheeler et al. (2009) reveals weak maxima in the direction of WBV, whereas analyses on low-angle boundaries reveal a strong maxima of WBV with **b** = [100].

Multiple bands of small grains are observed in some of the crystals deformed under hydrous conditions. These bands are subparallel to the rotated edge of the crystal, meaning that they have the orientation that a strain marker placed perpendicular to the shear direction would have. The small grains in the bands have large distributions of crystallographic orientations but have a maxima similar to that of the parent crystal orientation as presented in Figure 6.

### 3.3. FTIR Analyses

Results of unpolarized FTIR spectra are presented in Figure 7. Significant hydrogen incorporation into the crystal lattice is apparent, yielding a concentration of ~320 ppm H/Si. Peaks in the Absorption Coefficient are most pronounced at wavenumbers of 3,573, 3,526, and 3,229 $cm^{-1}$. These peak positions are similar to that of experimentally hydrated San Carlos olivine, except that the minor peaks at 3,357 and 3,328 are less pronounced in the hydrated olivine from Pakistan.

**Table 2**
*EPMA Results*

| Oxide | Pak 1 (wt. %) | Pak 3 (wt. %) |
|---|---|---|
| MgO | 48.36 | 49.08 |
| $SiO_2$ | 40.84 | 41.36 |
| FeO | 10.53 | 8.92 |
| $Al_2O_3$ | 0.02 | 0.02 |
| CaO | 0.08 | 0.09 |
| $TiO_2$ | 0.00 | 0.00 |
| NiO | 0.35 | 0.37 |
| MnO | 0.14 | 0.13 |
| Total | 100.34 | 99.97 |

*Note.* EPMA = Electron probe microanalyses.

### 3.4. EPMA Analyses

The results from EPMA analyses are presented in Table 2. The average value of Fo# ($100 * (Mg/(Mg + Fe))$) is 89 and 91 for Pak1 and Pak3 crystals, respectively. Trace amounts of Ni, Ca, and Al are also present and Ti concentrations were generally below the detection limit for our EPMA analyses.

## 4. Discussion

### 4.1. Mechanical Data

The mechanical data presented in Figure 4 give insight into the underlying physical processes that control hydrolytic weakening for crystals deformed by the motion of dislocations on different slip systems. The data from crystals deformed under anhydrous conditions reveal larger values of $n$ compared to those deformed under hydrous conditions. Generally, olivine deforming by the motion of dislocations at $T > 1100$ °C and stress <300 MPa exhibits values of $n$ between ~2.5 and ~4, consistent with deformation where most of the strain is accommodated by the glide of dislocations but the strain rate is limited by the rate of climb (Hirth & Kohlstedt, 2015). However, the values of $n$ observed for crystals deformed under anhydrous conditions in Figure 4 exceed those commonly observed values. The large values of $n$ for crystals deformed under anhydrous conditions, especially the values of $n \approx 5.3$ for those oriented to activate the (010)[100] slip system, suggesting that deformation may occur in a glide-controlled regime.

In contrast, all crystals deformed under hydrous conditions reveal mechanical behavior with $n \leq 3.5$. Although the relatively small range of shear stresses and shear strain rates explored for crystals deformed under hydrous conditions in this study makes it difficult to precisely constrain the values of $n$, it is clear from the results presented in Figure 4 that $n$ is close to and probably lower than 3.5. A small range of shear stress and shear strain rate was used as low shear stresses and strain rates require long experiments that increase the risk of losing water to the confining argon gas and high shear stresses and strain rates increase the risk of slipping on the interfaces between the crystal and the shear pistons. The strain rate of crystals deforming under hydrous conditions is less stress sensitive than the strain rate of those deformed under anhydrous conditions, which is broadly consistent with the previous results on olivine single crystals (e.g., Mackwell et al., 1985; Tielke et al., 2017) and polycrystalline olivine (e.g., Carter & Ave'Lallemant, 1970; Karato et al., 1986). The observed differences in both the rate of deformation and values of $n$ between crystals deformed under anhydrous compared to those deformed under hydrous conditions suggest that different microphysical processes control the rate of deformation under the different conditions.

A comparison of the values of shear stress needed to deform crystals oriented for deformation on the different slip systems at a strain rate of $10^{-5}$ $s^{-1}$ and at 1300 °C is presented in Table 3. The ratio of shear stress needed to deform crystals under anhydrous conditions to that needed to deform under hydrous conditions ranges from 3.0 for crystals oriented to activate dislocations on the (001)[100] slip system to 1.4 for those oriented to activate dislocations on the (100)[001] slip system. Crystals oriented for shear on the (001)[100] slip system reveal a larger weakening effect compared to crystals in deformed compression with the applied stress at 45° to the [100] and [001] crystallographic axes (i.e., the $[101]_c$ orientation) from Mackwell et al. (1985). However, the magnitude of weakening of crystals oriented for the (010)[100] slip system is similar to that

**Table 3**
*Strength of Slip Systems at an Equivalent Strain Rate of* $10^{-5}$ $s^{-1}$

| Slip system | $\tau$ (MPa) dry | $\tau$ (MPa) wet | $\frac{\tau_{dry}}{\tau_{wet}}$ | CRSS dry[a] | CRSS wet[a] |
|---|---|---|---|---|---|
| (010)[100][b] | 66.6 | 34.3 | 1.9 | 1.3 | 2.0 |
| (001)[100] | 51.9 | 17.1 | 3.0 | 1.0 | 1.0 |
| (100)[001] | 53.1 | 37.2 | 1.4 | 1.0 | 2.2 |
| (010)[001][c] | 171 | 67.5 | 2.5 | 3.3 | 3.9 |

*Note.* CRSS = critical resolved shear stress.
[a]Values of CRSS are normalized to that of weakest slip system, which was the (001)[100] for each condition. [b]Data normalized from 1250 to 1300 °C using the activation energies for wet and dry dislocation creep from Hirth and Kohlstedt (2003). [c]Data for (010)[001] are from Experiments 4865 and 4868 for $[011]_c$ from Mackwell et al. (1985) converted to shear values using the relationships in Appendix A.

for crystals deformed in compression with the applied stress at 45° to the [100] and [010] crystallographic axes (i.e., the $[110]_c$ orientation) from Mackwell et al. (1985). Overall, the amount of hydrogen-induced weakening in shear experiments from this study is in reasonable agreement with Mackwell et al. (1985).

The different amount of weakening in crystals in different orientations may be explained using a climb-controlled model of dislocation creep that follows the form of equation (1). Climb requires the nucleation of jogs, which is dependent on hydrogen concentration (Hobbs, 1984; Kohlstedt & Hansen, 2015), and jogs on the different slip systems may nucleate at different rates as a function of hydrogen content. Diffusivity of hydrogen in olivine is strongly anisotropic, whether occurring by a proton-electron hole mechanism (Mackwell & Kohlstedt, 1990) or a proton-vacancy mechanism (Demouchy & Mackwell, 2006). Conversely, silicon diffusivity is largely considered to be isotropic (e.g., Costa & Chakraborty, 2008), but almost all of the data for silicon diffusivity are for measurements made parallel to the [001] crystallographic direction. It is possible that silicon diffusivity and jog nucleation are strongly anisotropic in olivine, which would explain the observed orientation-dependent weakening between crystals deformed under anhydrous and hydrous conditions in Table 3.

Changes in the rate-limiting mechanism when transitioning from anhydrous to hydrous conditions may explain the different hydrogen sensitivities of the different slip systems. Under anhydrous conditions, the relative strength of the slip systems may be controlled by either dislocation climb that is controlled by pipe diffusion or dislocation glide that is rate limited by the ability of dislocations to move through obstacles. However, at conditions of higher water fugacity, the rate-limiting process becomes the rate of climb, likely controlled by diffusion of silicon through the olivine lattice (e.g., Tielke et al., 2017) and the relative strength of the slip systems becomes controlled by anisotropy in jog nucleation.

An alternative interpretation is that dislocation motion is always rate limited by glide of dislocations and controlled by the Peierls stress, which may be influenced by hydrogen. Under this hypothesis, hydrogen ions would interact with adjacent bonds in the lattice in different ways, which in turn may control the relative strengths of the dislocation slip systems. This hypothesis has been proposed to operate for quartz (Griggs, 1967), olivine (Karato et al., 2008; Katayama & Karato, 2008), and MgO (Skelton & Walker, 2018). Recent transmission electron microscopy observations on olivine deformed in a multianvil apparatus reveal that larger populations of dislocations form on the (001)[100] slip system when deformation occurs under hydrous conditions compared to anhydrous conditions, which may be attributed to an anisotropic dependence of Peierls stress on water content (Wang et al., 2019). Additionally, The Peierls stress is directly related to elasticity and it has been shown that elastic properties of olivine in different directions change by different amounts with the addition of hydrogen (Jacobsen et al., 2008). Therefore, it might be expected that the Peierls stress changes with the addition of hydrogen by different amounts for different slip systems.

### 4.2. Interpretation of EBSD Measurements

Analyses of the EBSD map for a crystal deformed by the motion of dislocations on the (010)[100] slip system presented in Figure 5 are consistent with deformation where most of the strain is accommodated by the glide of dislocations. The absence of low-angle boundaries, in the interior of the grain suggests that (010)[100] dislocations move unimpeded through the crystal. However, low-angle boundaries that may be described by rotation about the [001] crystallographic axis develop at the edge of the crystal, which is consistent with the operation of the (010)[100] slip system (Prior et al., 2009). The preference for low-angle boundaries to organize at the edge of the crystal may be a result of the relatively low stress regions that result from a change in boundary conditions at the edge of the crystal.

The occurrence of bands of small grains in Figure 6 are not likely to influence the mechanical behavior of the crystals. The orientation of the bands, which is consistent with that of a strain marker originally perpendicular to the shear direction, suggests that the bands of fine-grained material may have formed from fractures that developed before the onset of deformation (similar to Muto et al., 2011). The fractures may develop at the beginning of the experiment due to differences in thermal expansion between the olivine crystals and adjacent metals, such that a series of parallel fractures were generated normal to the shear direction. When high-temperature and high-pressure conditions were achieved, the fractures healed and residual fine-grained material may have formed compacted grains that experienced subsequent rotation. When a shear stress was applied at high-temperature conditions, the regions occupying former fractures were rotated along with the edge of the crystal due to the movement of dislocations in the crystal. Some of the small grains likely grew larger as deformation progressed. Importantly, at the small strains achieved in this study, the fine-grained bands act similar to strain markers placed inside deformation experiments (e.g., Jung et al., 2006) and are not expected to influence the mechanical behavior of the deforming single crystals.

### 4.3. Comparison of Pakistan Olivine to San Carlos Olivine

Previous workers sourced olivine from a variety of locations, as well as synthetically produced olivine, to study the physical properties of this important mineral. Some of the highest quality and largest olivine crystals have come from San Carlos, Arizona, making it an appealing material to use in experimental studies. Large inclusion-free olivine single crystals from this region are increasingly difficult to obtain. The challenges associated with obtaining gem quality olivine in sufficient size and quantity to carry out experimental studies has led to an increase in the use of olivine from other locations, such as the olivine from Pakistan used in this study. However, prior to this study, it had yet to be established that the physical properties of olivine from these two different locations are the same.

The exact location from which the olivine used in this study was sampled is not known, as the olivine was obtained from a gem dealer. A major source of gem quality olivine in Pakistan is near Sapat in Kohistan District. Previous EPMA analyses on olivine from Kohistan reveal major and minor element compositions nearly identical to the olivine used in this study (Gose et al., 2010). However, the FTIR spectrum for the olivine used in this study lack the absorbance peaks at wavenumbers between 3,800 and 3,000 $cm^{-1}$ observed in some olivine from Sapat (Gose et al., 2010). The differences in the FTIR spectra between these olivines highlights the importance of EPMA and FTIR characterization of the starting material before comparing results from the literature.

The results presented above provide an opportunity to compare the mechanical behavior and hydrogen incorporation mechanisms of olivine from Pakistan to that of San Carlos Arizona. The mechanical behavior of olivine crystals from different locations is in very good agreement as exemplified by Figure 4, where crystals from Pakistan oriented for deformation on the (001)[100] slip system under anhydrous conditions (red circles) deform at nearly the same shear stress as crystals from San Carlos Arizona (red squares) from Tielke, Zimmerman, et al. (2016). This observation suggests that the mechanical data for crystals oriented to activate the (010)[100], (001)[100], and (100)[001] slip systems may also be compared to the relatively large database of data from experiments carried out on San Carlos olivine. In addition, the similarity of postexperiment peak height and position in the FTIR spectra in Figure 7 suggests hydrogen is incorporated by the same mechanism in the two olivines from different localities.

### 4.4. Implication for LPO Development

In polycrystalline material deforming by dislocation creep, grains tend to preferentially align such that the Burgers vector of the weakest slip system is parallel to the direction of shear and the slip plane of the weakest slip system is parallel to the shear plane. Based on this principle, Jung et al. (2006) hypothesized that the

observed changes in LPO in polycrystalline olivine were a result in changes in the relative strengths of dislocation slip systems as a function of water content. However, until now, this hypothesis has not been directly tested because of limitations imposed by using a compression geometry to deform single crystals, where only two of the four dominant dislocation slip systems can be activated independently.

The results of this study are generally consistent with a water-dependent change in the nature of LPO in polycrystalline olivine. Polycrystalline olivine with low water content tends to form A-type or D-type LPO, where the [100] axes align parallel to the direction of shear and the [010] axes align normal to the shear plane or develops a girdle around the shear direction, respectively (e.g., Jung et al., 2006). These types of LPO suggest that the (010)[100] and (001)[100] slip systems are the weakest and have similar strengths, which is consistent with the results presented in Table 3. Polycrystalline olivine with moderate water content develops E-type LPO, where the [100] axis aligns parallel to the direction of shear and the [001] axis aligns normal to the shear plane. If the E-type LPO is formed by the motion of dislocations, the (001)[100] dislocation slip system should be the weakest and is much weaker than the other slip systems, which is consistent with the results presented in Table 3. In contrast, our mechanical data are not directly consistent with a transition from E-type LPO at moderate hydrogen content to C-type LPO at larger water content, which would necessitate a large degree of hydrolytic weakening on the (100)[001] slip system. However, the transition from E-type to C-type LPO occurs at much higher hydrogen content compared to those used in this study and it is likely that deformation at higher pressures and higher hydrogen content may be needed to observe that transition.

More quantitative models of LPO development are needed to couple the results of olivine deformation experiments with large-scale phenomena such as mantle flow. One of the most commonly used models of LPO development in mantle rocks is the viscoplastic self-consistent (VPSC) method (e.g., Boneh et al., 2015; Castelnau et al., 2008, 2009; Demouchy et al., 2014; Raterron et al., 2014; Tommasi et al., 2000; Wallis et al., 2019). Although the VPSC approach has limitations, such as restrictions in deformation geometry and coupling LPO development with precise predictions of mechanical evolution (Signorelli & Tommasi, 2015), it is a useful tool for predicting LPO development in olivine-rich rocks.

VPSC models require knowledge of the relative strength of the slip systems in a material, which is often carried out by defining a critical resolved shear stress (CRSS) for each slip system. The CRSS describes the stress needed to move dislocations for a given strain rate on a specific slip system and is generally normalized to the weakest slip system, such that values of 1 indicate weak slip systems and larger values indicate stronger slip systems. Normalized values of CRSS for olivine crystals deformed under either anhydrous or hydrous conditions and normalized to a temperature of 1300 °C are presented in Table 3. CRSS values from crystals deformed under anhydrous conditions indicate small values for the (010)[100], (001)[100], and (100)[001] slip systems and relatively large values of CRSS for the (010)[001] slip system. These predict the formation of A- or D-type LPO in polycrystalline olivine deformed under anhydrous conditions, which is consistent with high-strain deformation of olivine aggregates (e.g., Bystricky et al., 2000; Zhang & Karato, 1995). Similar types of LPO have been also observed in olivine and olivine + orthopyroxene aggregates deforming by grain-size-sensitive mechanisms (Hansen et al., 2012; Miyazaki et al., 2013; Tasaka, Zimmerman, & Kohlstedt, 2017, Tasaka, Zimmerman, Kohlstedt, Stünitz, et al., 2017; Tielke, Hansen, et al., 2016), highlighting the need for gaining deeper understanding of the role of grain boundaries in LPO development. In contrast, crystals deformed under hydrous conditions reveal that the (001)[100] slip system has much lower CRSS values compared to the other slip systems. The CRSS values for olivine crystals deformed under hydrous conditions are more consistent with the formation of E-type LPO in hydrous polycrystalline olivine, which is broadly consistent with high-strain deformation experiments on olivine aggregates carried out under hydrous conditions (e.g., Jung et al., 2006; Tasaka et al., 2016).

## 5. Conclusions

Hydrolytic weakening of olivine single crystals was measured for crystals sheared in three different orientations. The chemical composition, mechanical behavior, and infrared spectra of olivine from Pakistan is very similar to that from San Carlos, Arizona. Crystals sheared to activate the (001)[100] dislocation slip system display the largest amount of hydrolytic weakening, which is consistent with a dislocation mechanism being responsible for the transition from A-type or D-type (where [100] axes align parallel with shear direction and the [010] axes either align perpendicular to the shear plane or form a girdle perpendicular to the

shear direction) LPO under anhydrous conditions to E-type LPO (where the [100] axes orient close to the shear direction and the (001) planes are preferentially oriented parallel to the shear plane) under hydrous conditions in polycrystalline olivine. Experiments at higher pressure, and therefore higher water fugacity conditions, are needed to elucidate the transition from E-type to C-type LPO.

## Appendix A: Correction for Stress Supported by Metal

Deformation experiments in a gas-medium apparatus necessarily involves placing metal around the deforming sample. These metals serve several purposes. An iron tube goes along the length of the assembly to prevent argon from leaking out between the ceramic pistons or between the sample and the ceramic pistons, nickel sleeves hold the sample in position between the lanthanated tungsten until they are held together by pressure, and a stainless steel capsule is used to keep water and hydrogen in the assembly at high-temperature conditions.

To correct the mechanical data for the amount of stress supported by these metals, we first determine the shear strain rate at steady-state conditions. This value of shear strain rate is then used to solve for the shear stress supported by the different metal material using the published flow laws of Frost and Ashby (1982). The flow laws for nickel and gamma-iron involve an effective diffusion term, which necessitates using the dissection method to iteratively solve for stress. However, the published flow law for 316 stainless steel only includes a lattice diffusion term.

Initial attempts to correct the 316 stainless steel flow law from Frost and Ashby (1982) yielded large corrections in stress, even when the effect of effective diffusion was approximated using the values of pipe diffusion for gamma-iron. When this correction was applied to data from experiments performed using a stainless steel capsule, values of stresses calculated for some experiments were negative, indicating the flow law for stainless steel was over predicting the strength of the material and the stress correction for stainless steel was too large. Therefore, we performed a compression experiment on stainless steel to determine a flow law that could be applied to the jacket correction. The resultant constitutive equation for 316 stainless steel is

$$\dot{\epsilon} = 10^{4.00\pm0.69}\sigma^{4.5\pm0.3}\exp\left(\frac{-365\pm28\ \text{kJ/mol}}{RT}\right), \tag{A1}$$

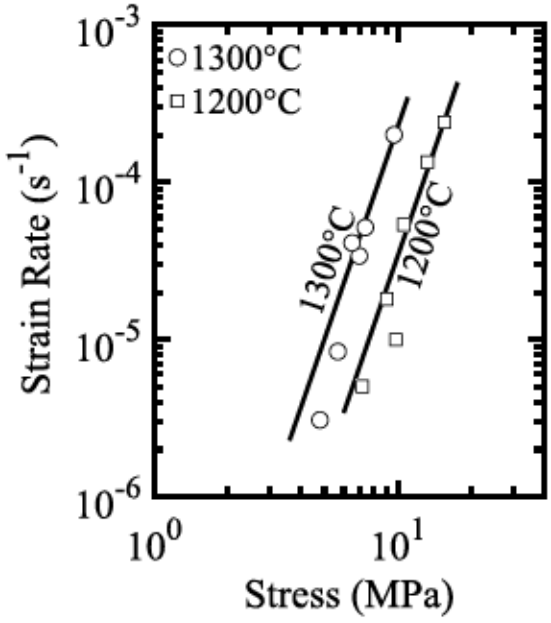


**Figure A1.** Strain rate as a function of stress for the stainless steel used as capsule material in hydrous experiments. The data points were corrected for the gamma-iron jacket, and the lines represent the constitutive equation presented in equation (A1).

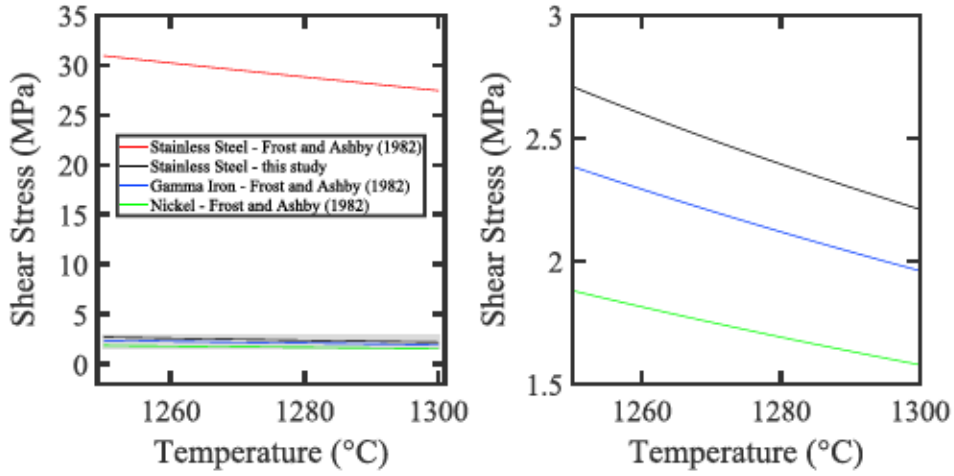


**Figure A2.** Shear stress as a function of temperature for metals used in experiments. All data are for a shear strain rate of $10^{-5}$ $s^{-1}$. The plot on the left is for all metals, and the plot on the right is for the data in the gray box in the plot on the left. Notice that the flow law for 316 steel from Frost and Ashby (1982), plotted as red, predicts much larger stresses required to deform compared to the stainless steel flow law in equation (A1) as well as the published flow laws for nickel and gamma-iron. We used the flow law for stainless steel (represented by the black line) because the stainless steel flow law from Frost and Ashby (1982) would result in too large of a jacket correction for our experimental conditions.

**Table A1**
*Mechanical Data for Stainless Steel*

| $\sigma$ (MPa) | $\dot{\epsilon}$ ($s^{-1}$) | Temperature (°C) | Strain (%) |
|---|---|---|---|
| 4.8 | 3.1E−6 | 1300 | 0.25 |
| 5.7 | 8.4E−6 | 1300 | 0.74 |
| 7.0 | 3.4E−5 | 1300 | 1.02 |
| 7.4 | 5.2E−5 | 1300 | 0.98 |
| 9.7 | 2.0E−4 | 1300 | 2.79 |
| 6.5 | 4.1E−5 | 1300 | 1.69 |
| 7.2 | 5.0E−6 | 1200 | 0.13 |
| 9.0 | 1.8E−5 | 1200 | 0.34 |
| 10.6 | 5.4E−5 | 1200 | 0.66 |
| 13.2 | 1.3E−4 | 1200 | 1.62 |
| 15.5 | 2.4E−4 | 1200 | 1.15 |
| 9.8 | 1.0E−5 | 1200 | 0.26 |

where $\dot{\epsilon}$ is the axial strain rate in per second and $\sigma$ is stress in megapascals. The results of the fit are in general agreement with the mechanical data for 316 stainless steel as presented in Figure A1. The flow law was converted to shear values for the stress correction using von Mises equivalent values assuming constant volume and no strain occurs in the orientation normal to the plane containing the loading and shear directions. The resulting relationships are $\tau = \sigma/2$ and $\dot{\gamma} = 3\,\dot{\epsilon}/\sqrt{3}$, which were used in the jacket correction procedure.

A comparison of the constitutive equations for nickel, gamma-iron, and stainless steel from Frost and Ashby (1982) and the stainless steel flow law from our experiment is presented in Figure A2. The data for the stainless steel experiment are presented in Table A1.

**Acknowledgments**
This work greatly benefited from advice and conversations with Mark Zimmerman, David Kohlstedt, Miki Tasaka, Andrew Walker, and Joshua Muir. Technical assistance from Steven May, Rochelle Taylor, Heath Bagshaw, Carmel Pinnington, Sarah Henton de Angelis, and Jon Fellowes is greatly appreciated. This research was supported by NERC Grants NE/M000060/1 and NE/M001458/1 within the program "The Feedback between Volatiles and Mantle Dynamics." The manuscript was significantly improved by thoughtful reviews from David Wallis and an anonymous reviewer. In accordance with Data Accessibility policy for UK Research Council grant-supported research, the data sets used to generate the graphical presentations in this paper are publicly available from the UK National Geoscience Data Centre (www.bgs.ac.uk/services/ngdc).

## References

Bachmann, F., Hielscher, R., & Schaeben, H. (2010). Texture analysis with MTEX—Free and open source software toolbox. *Solid State Phenomena*, *160*, 63–68.

Bai, Q., Mackwell, S., & Kohlstedt, D. (1991). High-temperature creep of olivine single crystals: 1. Mechanical results for buffered samples. *Journal of Geophysical Research*, *96*, 2441–2463. https://doi.org/10.1029/90JB01723

Bell, D., Rossman, G., Maldener, J., Endisch, D., & Rauch, F. (2003). Hydroxide in olivine: A quantitative determination of the absolute amount and calibration of the ir spectrum. *Journal of Geophysical Research*, *108*(B2), 2105. https://doi.org/10.1029/2001JB000679

Boneh, Y., Morales, L. F., Kaminski, E., & Skemer, P. (2015). Modeling olivine CPO evolution with complex deformation histories: Implications for the interpretation of seismic anisotropy in the mantle. *Geochemistry, Geophysics, Geosystems*, *16*, 3436–3455. https://doi.org/10.1002/2015GC005964

Bystricky, M., Kunze, K., Burlini, L., & Burg, J. P. (2000). High shear strain of olivine aggregates: Rheological and seismic consequences. *Science*, *290*(5496), 1564–1567. https://doi.org/10.1126/science.290.5496.1564

Carter, N. L., & Ave'Lallemant, H. G. (1970). High temperature flow of dunite and peridotite. *Geological Society of America Bulletin*, *81*(8), 2181–2202.

Castelnau, O., Blackman, D. K., & Becker, T. W. (2009). Numerical simulations of texture development and associated rheological anisotropy in regions of complex mantle flow. *Geophysical Research Letters*, *36*, L12304. https://doi.org/10.1029/2009GL038027

Castelnau, O., Blackman, D., Lebensohn, R., & Castañeda, P. (2008). Micromechanical modeling of the viscoplastic behavior of olivine. *Journal of Geophysical Research*, *113*, B09202. https://doi.org/10.1029/2007JB005444

Chopra, P., & Paterson, M. (1984). The role of water in the deformation of dunite. *Journal of Geophysical Research*, *89*(B9), 7861–7876.

Cooper, R. F., Stone, D. S., & Plookphol, T. (2016). Load relaxation of olivine single crystals. *Journal of Geophysical Research: Solid Earth*, *121*, 7193–7210. https://doi.org/10.1002/2016JB013425

Costa, F., & Chakraborty, S. (2008). The effect of water on Si and O diffusion rates in olivine and implications for transport properties and processes in the upper mantle. *Physics of the Earth and Planetary Interiors*, *166*(1), 11–29.

Demouchy, S., & Mackwell, S. (2006). Mechanisms of hydrogen incorporation and diffusion in iron-bearing olivine. *Physics and Chemistry of Minerals*, *33*(5), 347–355.

Demouchy, S., Mussi, A., Barou, F., Tommasi, A., & Cordier, P. (2014). Viscoplasticity of polycrystalline olivine experimentally deformed at high pressure and 900 °C. *Tectonophysics*, *623*, 123–135.

Demouchy, S., Tommasi, A., Ballaran, T. B., & Cordier, P. (2013). Low strength of Earth's uppermost mantle inferred from tri-axial deformation experiments on dry olivine crystals. *Physics of the Earth and Planetary Interiors*, *220*, 37–49.

Dohmen, R., Chakraborty, S., & Becker, H. (2002). Si and O diffusion in olivine and implications for characterizing plastic flow in the mantle. *Geophysical Research Letters*, *29*(21), 2030. https://doi.org/10.1029/2002GL015480

Durham, W. B., & Goetze, C. (1977). Plastic flow of oriented single crystals of olivine: 1. Mechanical data. *Journal of Geophysical Research*, *82*(36), 5737–5753. https://doi.org/10.1029/JB082i036p05737

Evans, B., & Goetze, C. (1979). The temperature variation of hardness of olivine and its implication for polycrystalline yield stress. *Journal of Geophysical Research*, *84*(B10), 5505–5524. https://doi.org/10.1029/JB084iB10p05505

Frost, H., & Ashby, M. (1982). *Deformation mechanism maps*. New York: Pergamon Press.

Girard, J., Chen, J., Raterron, P., & Holyoke, C. W. (2013). Hydrolytic weakening of olivine at mantle pressure: Evidence of [100](010) slip system softening from single-crystal deformation experiments. *Physics of the Earth and Planetary Interiors*, *216*, 12–20.

Gose, J., Schmädicke, E., Markowitz, M., & Beran, A. (2010). OH point defects in olivine from Pakistan. *Mineralogy and Petrology*, *99*(1-2), 105–111.

Griggs, D. (1967). Hydrolytic weakening of quartz and other silicates. *Geophysical Journal International*, *14*(1-4), 19–31.

Hansen, L. N., Conrad, C. P., Boneh, Y., Skemer, P., Warren, J. M., & Kohlstedt, D. L. (2016). Viscous anisotropy of textured olivine aggregates: 2. Micromechanical model. *Journal of Geophysical Research: Solid Earth*, *121*, 7137–7160. https://doi.org/10.1002/2016JB013240

Hansen, L., Zimmerman, M., & Kohlstedt, D. (2012). The influence of microstructure on deformation of olivine in the grain-boundary sliding regime. *Journal of Geophysical Research*, *117*, B09201. https://doi.org/10.1029/2012JB009305

Hess, H. H. (1964). Seismic anisotropy of the uppermost mantle under oceans. *Nature*, *203*, 629–631. https://doi.org/10.1038/203629a0

Hirth, G., & Kohlstedt, D. (2003). Rheology of the mantle wedge, *Inside the subduction factory* (Vol. 138, pp. 83–105).

Hirth, G., & Kohlstedt, D. (2015). The stress dependence of olivine creep rate: Implications for extrapolation of lab data and interpretation of recrystallized grain size. *Earth and Planetary Science Letters*, *418*, 20–26.

Hobbs, B. (1984). Point defect chemistry of minerals under a hydrothermal environment. *Journal of Geophysical Research*, *89*(B6), 4026–4038.

Holtzman, B., Kohlstedt, D., Zimmerman, M., Heidelbach, F., Hiraga, T., & Hustoft, J. (2003). Melt segregation and strain partitioning: Implications for seismic anisotropy and mantle flow. *Science*, *301*(5637), 1227–1230.

Idrissi, H., Bollinger, C., Boioli, F., Schryvers, D., & Cordier, P. (2016). Low-temperature plasticity of olivine revisited with in situ TEM nanomechanical testing. *Science Advances*, *2*(3), e1501671.

Ismail, W. B., & Mainprice, D. (1998). An olivine fabric database: An overview of upper mantle fabrics and seismic anisotropy. *Tectonophysics*, *296*(1-2), 145–157. https://doi.org/10.1016/S0040-1951(98)00141-3

Jacobsen, S. D., Jiang, F., Mao, Z., Duffy, T. S., Smyth, J. R., Holl, C. M., & Frost, D. J. (2008). Effects of hydration on the elastic properties of olivine. *Geophysical Research Letters*, *35*, L14303. https://doi.org/10.1029/2008GL034398

Jung, H., & Karato, S. (2001). Water-induced fabric transitions in olivine. *Science*, *293*(5534), 1460–1462.

Jung, H., Katayama, I., Jiang, Z., Hiraga, I., & Karato, S. (2006). Effect of water and stress on the lattice-preferred orientation of olivine. *Tectonophysics*, *421*(1–2), 1–22.

Jung, H., Lee, J., Ko, B., Jung, S., Park, M., Cao, Y., & Song, S. (2013). Natural type-C olivine fabrics in garnet peridotites in North Qaidam UHP collision belt, NW China. *Tectonophysics*, *594*, 91–102.

Karato, S., Jung, H., Katayama, I., & Skemer, P. (2008). Geodynamic significance of seismic anisotropy of the upper mantle: New insights from laboratory studies. *Annual Review of Earth and Planetary Sciences*, *36*, 59–95.

Karato, S., Paterson, M. S., & FitzGerald, J. D. (1986). Rheology of synthetic olivine aggregates: Influence of grain size and water. *Journal of Geophysical Research*, *91*(B8), 8151–8176.

Katayama, I., & Karato, S. (2008). Low-temperature, high-stress deformation of olivine under water-saturated conditions. *Physics of the Earth and Planetary Interiors*, *168*(3), 125–133.

Kneller, E. A., Van Keken, P. E., Karato, S.-i., & Park, J. (2005). B-type olivine fabric in the mantle wedge: Insights from high-resolution non-Newtonian subduction zone models. *Earth and Planetary Science Letters*, *237*(3-4), 781–797.

Kneller, E., Van Keken, P., Katayama, I., & Karato, S.-i. (2007). Stress, strain, and b-type olivine fabric in the fore-arc mantle: Sensitivity tests using high-resolution steady-state subduction zone models. *Journal of Geophysical Research*, *112*, B04406. https://doi.org/10.1029/2006JB004544

Kohlstedt, D. (2006). The role of water in high-temperature rock deformation. *Reviews in mineralogy and geochemistry*, *62*(1), 377–396.
Kohlstedt, D., & Goetze, C. (1974). Low-stress high-temperature creep in olivine single crystals. *Journal of Geophysical Research*, *79*(14), 2045–2051.
Kohlstedt, D., & Hansen, L. (2015). Constitutive equations, rheological behavior, and viscosity of rocks. *Treatise on Geophysics*, *2*, 441–472.
Kumamoto, K. M., Thom, C. A., Wallis, D., Hansen, L. N., Armstrong, D. E., Warren, J. M., et al. (2017). Size effects resolve discrepancies in 40 years of work on low-temperature plasticity in olivine. *Science Advances*, *3*(9), e1701338.
Mackwell, S., & Kohlstedt, D. (1990). Diffusion of hydrogen in olivine: Implications for water in the mantle. *Journal of Geophysical Research*, *95*(B4), 5079–5088.
Mackwell, S., Kohlstedt, D., & Paterson, M. (1985). The role of water in the deformation of olivine single crystals. *Journal of Geophysical Research*, *90*(B13), 11,319–11,333.
Mei, S., & Kohlstedt, D. L. (2000). Influence of water on plastic deformation of olivine aggregates: 2. Dislocation creep regime. *Journal of Geophysical Research*, *105*, 21,471–21,481.
Michibayashi, K., & Oohara, T. (2013). Olivine fabric evolution in a hydrated ductile shear zone at the Moho Transition Zone, Oman Ophiolite. *Earth and Planetary Science Letters*, *377*, 299–310.
Miyazaki, T., Sueyoshi, K., & Hiraga, T. (2013). Olivine crystals align during diffusion creep of Earth's upper mantle. *Nature*, *502*(7471), 321–326.
Muto, J., Hirth, G., Heilbronner, R., & Tullis, J. (2011). Plastic anisotropy and fabric evolution in sheared and recrystallized quartz single crystals. *Journal of Geophysical Research*, *116*, B02206. https://doi.org/10.1029/2010JB007891
Nicolas, A., & Christensen, N. I. (1987). Formation of anisotropy in upper mantle peridotites—A review. *Composition, Structure and Dynamics of the Lithosphere-asthenosphere System*, *16*, 111–123.
Park, Y., & Jung, H. (2015). Deformation microstructures of olivine and pyroxene in mantle xenoliths in Shanwang, eastern China, near the convergent plate margin, and implications for seismic anisotropy. *International Geology Review*, *57*(5-8), 629–649.
Paterson, M. S. (1982). The determination of hydroxyl by infrared absorption in quartz, silicate glasses and similar materials. *Bulletin de la Societe Francaise de Minéralogie*, *105*(1), 20–29.
Paterson, M. S. (1990). Rock deformation experimentation, *The brittle ductile transition in rocks: The Heard volume* (Vol. 56, pp. 187–194).
Poe, B. T., Romano, C., Nestola, F., & Smyth, J. R. (2010). Electrical conductivity anisotropy of dry and hydrous olivine at 8 GPa. *Physics of the Earth and Planetary Interiors*, *181*(3-4), 103–111.
Poirier, J.-P. (1985). *Creep of crystals: High-temperature deformation processes in metals, ceramics and minerals*. New York: Cambridge University Press.
Pommier, A., Kohlstedt, D. L., Hansen, L. N., Mackwell, S., Tasaka, M., Heidelbach, F., & Leinenweber, K. (2018). Transport properties of olivine grain boundaries from electrical conductivity experiments. *Contributions to Mineralogy and Petrology*, *173*, 1–13.
Prior, D. J., Mariani, E., & Wheeler, J. (2009). Ebsd in the Earth sciences: Applications, common practice, and challenges, *Electron backscatter diffraction in materials science* (pp. 345–360). Boston, MA: Springer.
Raitt, R. W. (1969). *Anisotropy of the upper mantle* (pp. 250–256). Washington, DC: American Geophysical Union (AGU). https://doi.org/10.1029/GM013p0250
Raterron, P., Amiguet, E., Chen, J., Li, L., & Cordier, P. (2009). Experimental deformation of olivine single crystals at mantle pressures and temperatures. *Physics of the Earth and Planetary Interiors*, *172*(1-2), 74–83. https://doi.org/10.1016/j.pepi.2008.07.026
Raterron, P., Chen, J., Li, L., Weidner, D., & Cordier, P. (2007). Pressure-induced slip-system transition in forsterite: Single-crystal rheological properties at mantle pressure and temperature. *American Mineralogist*, *92*(8-9), 1436–1445.
Raterron, P., Detrez, F., Castelnau, O., Bollinger, C., Cordier, P., & Merkel, S. (2014). Multiscale modeling of upper mantle plasticity: From single-crystal rheology to multiphase aggregate deformation. *Physics of the Earth and Planetary Interiors*, *228*, 232–243.
Signorelli, J., & Tommasi, A. (2015). Modeling the effect of subgrain rotation recrystallization on the evolution of olivine crystal preferred orientations in simple shear. *Earth and Planetary Science Letters*, *430*, 356–366.
Skelton, R., & Walker, A. M. (2018). Lubrication of dislocation glide in MgO by hydrous defects. *Physics and Chemistry of Minerals*, *45*, 713–726.
Skemer, P., Warren, J. M., Hansen, L. N., Hirth, G., & Kelemen, P. B. (2013). The influence of water and LPO on the initiation and evolution of mantle shear zones. *Earth and Planetary Science Letters*, *375*, 222–233.
Tasaka, M., Michibayashi, K., & Mainprice, D. (2008). B-type olivine fabrics developed in the fore-arc side of the mantle wedge along a subducting slab. *Earth and Planetary Science Letters*, *272*(3-4), 747–757.
Tasaka, M., Zimmerman, M. E., & Kohlstedt, D. L. (2016). Evolution of the rheological and microstructural properties of olivine aggregates during dislocation creep under hydrous conditions. *Journal of Geophysical Research: Solid Earth*, *121*, 92–113. https://doi.org/10.1002/2015JB012134
Tasaka, M., Zimmerman, M. E., & Kohlstedt, D. L. (2017). Rheological weakening of olivine + orthopyroxene aggregates due to phase mixing: 1. Mechanical behavior. *Journal of Geophysical Research: Solid Earth*, *122*, 7584–7596. https://doi.org/10.1002/2017JB014333
Tasaka, M., Zimmerman, M. E., Kohlstedt, D. L., Stünitz, H., & Heilbronner, R. (2017). Rheological weakening of olivine + orthopyroxene aggregates due to phase mixing: Part 2. Microstructural development. *Journal of Geophysical Research: Solid Earth*, *122*, 7597–7612. https://doi.org/10.1002/2017JB014311
Tielke, J. A., Hansen, L. N., Tasaka, M., Meyers, C., Zimmerman, M. E., & Kohlstedt, D. L. (2016). Observations of grain size sensitive power law creep of olivine aggregates over a large range of lattice-preferred orientation strength. *Journal of Geophysical Research: Solid Earth*, *121*, 506–516. https://doi.org/10.1002/2015JB012302
Tielke, J. A., Zimmerman, M. E., & Kohlstedt, D. L. (2016). Direct shear of olivine single crystals. *Earth and Planetary Science Letters*, *455*, 140–148.
Tielke, J. A., Zimmerman, M. E., & Kohlstedt, D. L. (2017). Hydrolytic weakening in olivine single crystals. *Journal of Geophysical Research: Solid Earth*, *122*, 3465–3479. https://doi.org/10.1002/2017JB014004
Tommasi, A., Mainprice, D., Canova, G., & Chastel, Y. (2000). Viscoplastic self-consistent and equilibrium-based modeling of olivine lattice preferred orientations: Implications for the upper mantle seismic anisotropy. *Journal of Geophysical Research*, *105*, 7893–7908. https://doi.org/10.1029/1999JB900411
Wallis, D., Hansen, L., Tasaka, M., Kumamoto, K., Parsons, A., Lloyd, G., et al. (2019). The impact of water on slip system activity in olivine and the formation of bimodal crystallographic preferred orientations. *Earth and Planetary Science Letters*, *508*, 51–61.
Wang, L., Miyajima, N., Kawazoe, T., & Katsura, T. (2019). Activation of [100](001) slip system by water incorporation in olivine and the cause of seismic anisotropy decrease with depth in the asthenosphere. *American Mineralogist*, *104*(1), 47–52.
Weertman, J. (1955). Theory of steady-state creep based on dislocation climb. *Journal of Applied Physics*, *26*(10), 1213–1217.

Wheeler, J., Mariani, E., Piazolo, S., Prior, D., Trimby, P., & Drury, M. (2009). The Weighted Burgers Vector: A new quantity for constraining dislocation densities and types using electron backscatter diffraction on 2D sections through crystalline materials. *Journal of Microscopy*, *233*(3), 482–494.

Zhang, S., & Karato, S. (1995). Lattice preferred orientation of olivine aggregates deformed in simple shear. *Nature*, *375*(6534), 774–777.